JACS
JOURNAL OF THE AMERICAN CHEMICAL SOCIETY
pubs.acs.org/JACS
Article

Abundance of Low-Energy Oxygen Vacancy Pairs Dictates the Catalytic Performance of Cerium-Stabilized Zirconia

Yao Peng, Xia-Lan Si, Cheng Shang,* and Zhi-Pan Liu*

Cite This: https://doi.org/10.1021/jacs.4c01285
Read Online

ABSTRACT: Cerium-stabilized zirconia ($Ce_{1-x}Zr_xO_y$, CZO) is renowned for its superior oxygen storage capacity (OSC), a key property long believed to be beneficial to catalytic oxidation reactions. However, 50% Ce-containing CZO recorded with the highest OSC has disappointingly poor performance in catalytic oxidation reactions compared to those with higher Ce contents but lower OSC ability. Here, we employ global neural network (G-NN)-based potential energy surface exploration methods to establish the first ternary phase diagram for bulk structures of CZO, which identifies three critical compositions of CZO, namely, 50, 60, and 80% Ce-containing CZO that are thermodynamically stable under typical synthetic conditions. 50% Ce-containing CZO, although having the highest OSC, exhibits the lowest O vacancy (O_v) diffusion rate. By contrast, 60% Ce-containing CZO, despite lower OSC (33.3% OSC compared to that of 50% Ce-containing CZO), reaches the highest O_v diffusion ability and thus offers the highest CO oxidation catalytic performance. The physical origin of the high performance of 60% Ce-containing CZO is the abundance of energetically favorable O_v pairs along the ⟨110⟩ direction, which reduces the energy barrier of O_v diffusion in the bulk and promotes O_2 activation on the surface. Our results clarify the long-standing puzzles on CZO and point out that 60% Ce-containing CZO is the most desirable composition for typical CZO applications.

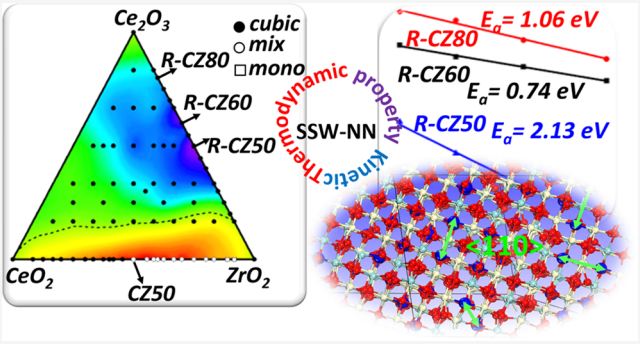

1. INTRODUCTION

The ceria−zirconia oxide (CZO) has gained significant prominence in heterogeneous catalysis for its high oxygen storage capacity (OSC)[1−6] and good thermal stability,[7,8] finding widespread use as either a direct catalyst or a support material for metal nanoparticles over the past few decades.[9−12] The CZO properties appear to be sensitive to the Ce/Zr ratio and thus the synthetic procedure in the experiment, which generates long-standing confusion on the correlation between OSC and catalytic performance. It is now established that the κ-phase 50% Ce-containing CZO[13] ($Ce_{0.5}Zr_{0.5}O_2$) has a groundbreaking OSC record (89% Ce^{4+} reduced to Ce^{3+}) but a low catalytic performance; the best CZO-supported metal catalyst generally requires a high Ce content (e.g., 80%).[14] Because of the lack of atomic-level knowledge of CZO structures, the finding of the best CZO in different applications is largely via trial-and-error tests. A theoretical guide to correlate the Ce/Zr ratio with its thermodynamics and kinetic properties is thus highly desirable.

As OSC was long believed to be the key descriptor for the catalytic performance of CZO, numerous efforts were devoted to identifying CZO with the highest OSC, which is defined to be the ability to release and store oxygen at the typical catalyst working conditions (e.g., below 773 K), $Ce_xZr_yO_z \rightarrow Ce_xZr_yO_{z-2n} + nO_2$. To date, 50% Ce-containing CZO, $Ce_{0.5}Zr_{0.5}O_2$, is most recognized as the composition with the highest OSC.[15−17] 50% Ce-containing CZO can be synthesized via the oxidation of the pyrochlore $Ce_{0.5}Zr_{0.5}O_{1.75}$ (a cubic crystal) precursor at 773 K in the air, which is first synthesized via the coprecipitation method at 1473 K under reducing conditions.[10,11] Later, an improved synthetic method, i.e., the solvent thermal method, was developed to prepare 50% Ce-containing CZO, which can exhibit even higher OSC than that synthesized by the coprecipitation method, suggesting the solvent thermal method can obtain a better crystalline cubic phase with fewer defects or other minority phases.[1] By density functional theory (DFT) calculations, Wang et al.[18] found that the lowest energy O vacancies (O_v) of cubic 50% Ce-containing CZO are all near Zr cations. It is therefore expected that the presence of defects or the random distribution of cations leads to a decrease in OSC. Indeed, many experiments showed that the synthetic method can influence the OSC

Received: January 26, 2024
Revised: March 31, 2024
Accepted: April 1, 2024

https://doi.org/10.1021/jacs.4c01285
J. Am. Chem. Soc. XXXX, XXX, XXX−XXX

markedly. For example, Madier et al. found that 63% Ce-containing CZO ($Ce_{0.63}Zr_{0.37}O_2$) prepared by the coprecipitation method under 1173 K has the largest OSC at 673 K,[19] while that of 50% Ce-containing CZO is only 10% under the same condition. On the contrary, when samples are pretreated with hydrothermal treatment and then calcined at 773 K, 50% Ce-containing CZO (OSC = 32%) is instead superior to 60% Ce-containing CZO (OSC = 24%), and the OSC of 50% Ce-containing CZO can be improved to 37% by increasing the temperature to 1173 K.[20] The improvement of the OSC of 50% Ce-containing CZO is accompanied by the enhancement of the main peak on the XRD patterns, which implies the importance of the purification and crystallization of the sample. Due to the lack of atomic-level knowledge of CZO with different compositions synthesized under different conditions, the correlation between the CZO Ce/Zr ratio, the atomic structure, and OSC ability is not established.

While the highest OSC ratio occurs at Ce contents of 50−63%, the best catalytic performance of CZO appears to shift to even higher Ce/Zr ratios, up to a Ce content of 80%. Taking CO oxidation as an example, where the light-off temperature (T_{50}) is often utilized as the measure of the catalyst activity, the T_{50} of the 50% Ce-containing CZO catalyst is reported to be above 688 K, while that of 75% Ce-containing CZO can be as low as 623 K, as shown by Meeyoo and co-worker. Not surprisingly, the catalyst activity is again sensitive to the catalyst preparation method. For the same 50% Ce-containing CZO, the catalyst prepared by the solvent thermal method (T_{50} = 688 K) is much more active than that prepared using the coprecipitation method (T_{50} > 873 K).[1] Consistently, the CO oxidation activity on the CZO (solvent thermal)-supported Pd catalyst (T_{50} = 362 K) is significantly higher than that on CZO (coprecipitation; T_{50} = 433 K). Importantly, Boaro et al. found that catalysts with higher activity also exhibited higher anion conductivity, suggesting that the diffusion rate of oxygen anions mattered in the catalytic cycle.[21] On the other hand, theoretical calculations suggested that CO oxidation involved O_2 activation at the surface O vacancy site[22−26] and the CO reaction with the surface O atom had a low barrier (e.g., 0.63 eV on Ce(111)).[27] The role of diffusion of O in bulk to the CO oxidation activity remains elusive.

The current puzzles on CZO can be largely attributed to the poor knowledge of the atomic structure of CZO, including cation positions and O_v distributions, under different synthetic conditions. Here, we present a comprehensive survey of the global potential energy surface of CZO bulk with various Ce/Zr molar ratios and oxidative states of Ce by using the SSW-NN method, i.e., stochastic surface walking (SSW) global optimization based on global neural network (G-NN) potential. The thermodynamic phase diagram and kinetic properties of key CZO compositions are then explored and quantified, and the catalytic CO oxidation on their surfaces is determined. We establish a quantitative correlation between the atomic structure of CZO and the properties, including the catalytic performance and the OSC, which should guide the future applications of CZO materials.

2. METHODS

2.1. G-NN Potential Generated from the SSW-NN Method. All simulations based on G-NN potential were carried out using the LASP code developed in our group, which implements data generation using SSW global optimization, G-NN training, and potential energy surface (PES) evaluation of G-NN potentials.[28−32] The Ce−Zr−O ternary G-NN potential was trained by self-learning the SSW global potential energy surface data set that covers a wide range of CZO compositions with different structural types, such as bulks, surfaces, and layers. More than 10^7 structures on CZO global PES were visited by SSW-NN during NN potential generation, and the final training data set of CZO consisted of 24552 structures that were selected to represent the global PES. The data set was calculated using plane-wave DFT calculations[33] as implemented in VASP (Vienna Ab-initio Simulation Package, see below). The training data set is available online.[34]

The G-NN potential has a five-layer (505-80-80-80-7) feed-forward MBNN architecture[35] for each element, in total containing 162081 fitting parameters. The details on the training data set are shown in Table S1 in the Supporting information (SI). The root-mean-square errors (RMSEs) for the energy and the force of the G-NN are 4.986 meV/atom and 0.130 eV/Å, respectively. This G-NN potential is now included in the G-NN library of LASP and available online.[36] We have also benchmarked the G-NN accuracy against the DFT results for important structures, which shows that the energy RMSE is 2.871 meV/atom for low-energy structures in this work (see Table S3 in the SI). This small error suggests that the G-NN PES is a good approximation of DFT PES and can be utilized to expedite the global structure search and pathway determination. It should be mentioned that with G-NN calculations to expedite PES exploration, all results reported in this work are finally converged using DFT calculations (see the following calculation setups).

2.2. DFT Calculations. The G-NN potential training relies on DFT calculated energy, forces, and stresses of structures.[28] To achieve high accuracy and data consistency, our DFT calculations in VASP utilized the following standard setups as utilized for generating all G-NN potentials in the LASP G-NN library: spin polarization is considered in the presence of the Ce element; the DFT functional is at the level of generalized gradient approximation (GGA-PBE);[37] the kinetic energy cutoff is 450 eV; the projector augmented wave (PAW) pseudopotential[38] is utilized to describe ionic core electrons; and the fully automatic Monkhorst−Pack K-mesh with 25 times the reciprocal lattice vectors[39] is used for the first Brillouin zone k-point sampling. To optimize the structure, we minimized the total energy until the total forces on each atom were less than 0.01 eV/Å. The inclusion of an onsite correlation term with the Hubbard U parameter (DFT + U) facilitates access to physical ground states of CZO, where the localized Ce 4f electrons were set to U = 5 eV in computing all energetics.[18,40] We also checked oxygen vacancy generation thermodynamics by using BEEF-vdW and PBE-D3 functionals,[41,42] which shows that the GGA-PBE provides the energetics most consistent with the known experiment (see page 10 in the SI).

2.3. Free-Energy Calculations. The free formation energy (ΔG_f) as defined in eq 1 is computed for evaluating the stability of CZO at each ratio, where the free energies of CeO_2, ZrO_2, O_2, and Ce_2O_3 are used as references. For solid states, since its vibration entropy and PV terms change very little, the free energy can be approximated by its DFT energy. For oxygen molecules, the free energy G_{O_2} includes DFT energy (E_{O_2}), zero-point energy (ZPE), and the standard gas-phase thermodynamic correction terms at varied temperatures.[43] The average O vacancy formation free energy $\Delta\mu$, as shown in the example of $Ce_{16}Zr_{16}O_{64}$, can be computed using eq 2 with reference to O_2 at 298 K and 1 atm pressure. The disproportionation energy (ΔG_d) of CZO between 60 and 80% Ce contents is calculated using eq 3. The adsorption energy of oxanes (ΔE_r) on surfaces is calculated using eq 4.

$$\Delta G_f(Ce_xZr_yO_n) = G_{Ce_xZr_yO_n} - xG_{CeO_2} - yG_{ZrO_2} + [(x+y) - n/2]G_{O_2} \quad (1)$$

$$G^{\theta}_{ad} = (G_{Ce_{16}Zr_{16}O_{56+n}} - G_{Ce_{16}Zr_{16}O_{56}})/n - \frac{n}{2}G^{\theta}_{O_2} \quad (2)$$

https://doi.org/10.1021/jacs.4c01285
J. Am. Chem. Soc. XXXX, XXX, XXX−XXX

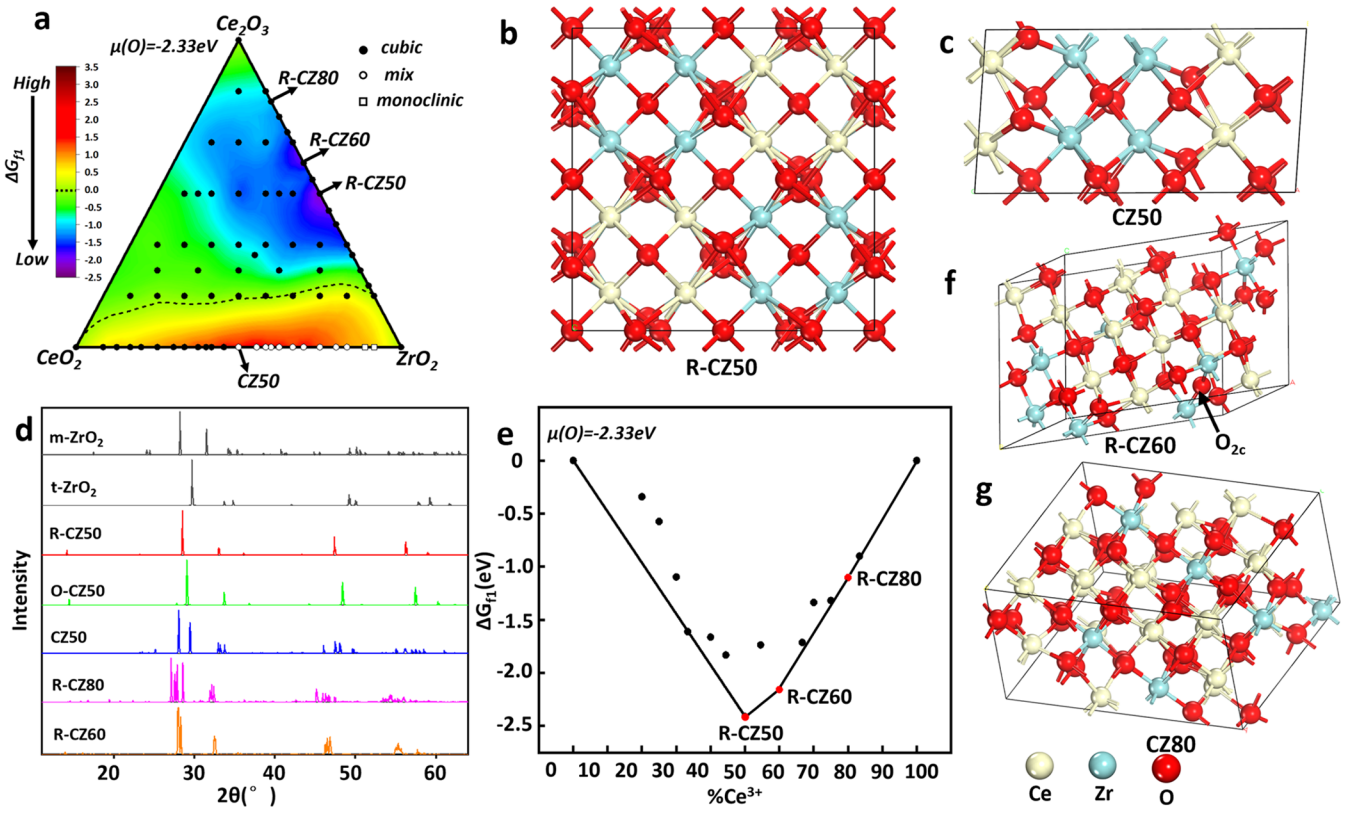

Figure 1. Energetics and atomic structures of CZO. (a) The Ce−Zr−O ternary phase diagram at the O chemical potential of −2.33 eV, equivalent to O_2 at 1800 K and ambient pressure. The color bar represents the formation energy of different compositions, where the area of negative and positive values is separated by a black dash curve. The cubic, mix, and monoclinic phases are labeled as solid circles, hollow circles, and squares, respectively. (b−g) The atomic structures of identified GM for R-CZ50, CZ50, R-CZ60, and R-CZ80. The interstitial oxygen atom is shown by arrows. (d) Simulated X-ray diffraction patterns of the GM structures that are compared with the standard ZrO_2 phases (tetragonal (t) and monoclinic (m) phases). (e) The thermodynamic convex hull diagram for $Ce_xZr_yO_{2y+3/2x}$, and three convex points R-CZ50, R-CZ60, and R-CZ80 are highlighted by red dots. Yellow balls: Ce atoms; cyan balls: Zr atoms; red balls: O atoms.

$$\Delta G_d = G_{Ce_xZr_yO_n} - mG_{Ce_{0.8}Zr_{0.2}O_{1.6}} - (1-m)G_{Ce_{0.6}Zr_{0.4}O_{1.7}} \quad (3)$$

$$\Delta E_r = (E_{co_2} - E_{co}) - (E_{surf+O} - E_{surf}) \quad (4)$$

2.4. Ionic Migration Simulation. The long-time MD simulations were carried out for three compositions, i.e., 50% Ce-containing CZO at a 2 × 2 × 2 periodic supercell built from $Ce_{16}Zr_{16}O_{56}$ (704 atoms in total), 60% Ce-containing CZO at a 2 × 4 × 2 supercell built from $Ce_{12}Zr_8O_{34}$(864 atoms in total), and 80% Ce-containing CZO at a 2 × 3 × 2 supercell built from $Ce_{24}Zr_6O_{48}$ (936 atoms in total). The initial structural relaxation was performed for 1 ns by using the isothermal−isobaric (NPT) ensemble at the target temperature to determine the equilibrium volume (lattice). The ion migration was then simulated using a Nose−Hoover thermostat[44,45] at the canonical ensemble with a time step of 1 fs. The first 0.3 ns of the NVT simulation was assigned to equilibrate the system, and the statistic average of the anion diffusion was calculated over the remaining time (up to 5 ns). For the purpose of analysis, the local relaxation was utilized to obtain the intrinsic structure for the structure snapshots taken from MD trajectories until the maximal force on the atom was below 0.01 eV/Å.

The Einstein relation was used to determine the oxygen diffusion coefficients (D) from the slopes of mean square displacements of the oxygen atom (Δr^2) plotted versus simulation time (t).

$$D = \lim_{t\to\infty} \frac{\langle \Delta r(t)^2 \rangle}{6t} \quad (5)$$

The activation energies for oxygen diffusion (E_a) were computed by fitting the calculated diffusion coefficients to the standard Arrhenius form using the following relation.

$$D = D_0 \exp\left(-\frac{E_a}{RT}\right) \quad (6)$$

The E_a values thereby obtained were used to characterize the dependence of the averaged diffusion barriers on different CZO compositions. The conductivity of oxygen ions σ was finally derived from the Nernst−Einstein relation with the diffusion coefficient D

$$\sigma = \frac{q^2 DN}{VN_a}\left(\frac{F^2}{RT}\right) \quad (7)$$

where N_a is the Avogadro constant, q is the charge of the mobile ion (2 for oxygen), N is the number of oxygen atoms, and F is Faraday's constant.

2.5. Surface Reaction Pathway Search. The slab model of CZO surfaces was used in calculating CO oxidation catalytic reactions. The slab model contains four O−M−O (M = Ce or Zr) layers, with the bottom two layers being fixed at the bulk-truncated position. The slab sizes of R-CZ50 and R-CZ60 are 13.19 × 7.61 Å with 90 atoms and 19.31 × 6.63 Å with 112 atoms, respectively. The vacuum regions of all these slabs are more than 25 Å. All of the transition states (TSs) were located using the double-ended surface walking method (DESW)[46] as implemented in LASP. G-NN calculations are utilized, if possible, e.g., those related to O diffusion containing only Ce, Zr, and O elements, to search for likely pathways and identify the lowest energy one. The TS is verified to have only one imaginary frequency, and the extrapolation from the TS to nearby minima is performed to confirm its relevance to the target reaction. DFT calculations are utilized to finally converge the lowest energy pathways. We also examined the dispersion effect on reactions by

https://doi.org/10.1021/jacs.4c01285
J. Am. Chem. Soc. XXXX, XXX, XXX−XXX

using PBE-D3[42] (see Figure S1 and Table S4 in the SI), which shows that the inclusion of dispersion little affects the CO oxidation kinetics.

3. RESULTS AND DISCUSSION

3.1. Thermodynamics of Ce−Zr−O Bulk Phases. Our investigation begins by thoroughly exploring the thermodynamic phase space, scanning likely bulk CZO structures with Ce/Zr/O ratios ranging from Ce_2O_x (x = 3−4) to ZrO_2, as mapped in the Ce−Zr−O ternary phase diagram with CeO_2, ZrO_2, and Ce_2O_3 being the three vertices (Figure 1a). We denote CZO bulk as $Ce_xZr_yO_n$, where the superscripts x, y, and n represent the concentrations of Ce, Zr, and O atoms, respectively. More than 70 compositions with different values of x and y were explored using SSW-NN, and after examining more than 10,000 minima at each composition, the corresponding global minima (GM) are obtained, as indicated by solid circles, hollow circles, and squares in Figure 1a (the chemical potential μ(O) (=1/2 G_{O_2}) equals to −2.33 eV, corresponding to the gas-phase O_2 at 1800 K, the temperature to synthesize the pyrochlore phase in the experiment[1]).

In general, the GM structure of CZO is influenced by both the Ce/Zr ratio and the Ce oxidation state (3^+ or 4^+). As depicted in Figure 1a, while most of the structures prefer the cubic phase (black dots),[47] the fully oxidized form, the oxides with Ce^{4+} and Zr^{4+} can exhibit different structures depending on the Ce^{4+}/Zr^{4+} ratio. They are cubic phase above 50%, become the mix phase (reflected as the phase junction of CeO_2 and ZrO_2 in the periodic supercell) from 50 to 11.1%, and finally shift to the monoclinic phase below 11.1% (the same as pure ZrO_2). The lattice parameters of four key GM with different Ce/Zr ratios are listed in Table 1, together with the coordination number of Ce and Zr in the bulk as elaborated in the following.

The black dashed curve in Figure 1a highlights the minima with formation energy below zero, which are mainly at the top-right part of the triangle, being close to the Ce_2O_3−ZrO_2 edge with the Ce/Zr ratio above 20%. The CZO along the Ce_2O_3−ZrO_2 edge are the reduced forms with 100% Ce^{3+} and thus named R-CZx (x = Ce content), hereafter, and their oxidized forms with the same lattice are named O-CZx. These O-CZx may not be the GM, since the filling of oxygen vacancies could change the energy landscape. In fact, the CeO_2−ZrO_2 edge (bottom of the triangle in Figure 1a), the oxidized form with 100% Ce^{4+}, gives the GM structure identified from SSW. As shown in Figure 1a, at high temperatures (1800 K), the Ce^{4+}-containing CZO samples are all unstable compared to Ce^{3+}-based CZO.

The most stable structure in Figure 1a is the reduced form, R-CZ50 (Figure 1b), known as the pyrochlore phase, a cubic structure (FD-3 M space group) with ΔG_f = −2.41 eV. The GM structure determined from SSW-NN is identical to that found in the experiment, and the structure has been analyzed previously by DFT.[18] In brief, R-CZ50 has all Ce 8-coordinated and Zr 6-coordinated, where all oxygen vacancies (O_v) are located at the tetrahedral void formed by four Zr cations[18] (O_v(4Zr)). Three types of oxygen are present, namely, O(4Zr) that coordinates with four Zr atoms, O(4Ce) that coordinates with four Ce atoms, and O(2Ce2Zr) that coordinates with two Zr and two Ce atoms.

By filling all O_v sites, R-CZ50 is then oxidized to O-CZ50, retaining the cubic lattice, which is the typical way to prepare 50% Ce-containing CZO in the experiment[10,11] This O-CZ50 is however no longer stable, as it is less energetically favored compared to CZ50 (GM from SSW), as indicated in the bottom edge of Figure 1a. CZ50 contains separated ZrO_2 and CeO_2 phases (mixed phase), gluing in a supercell of 24 atoms, with ΔG_f = +1.43 eV compared to the cubic CeO_2 phase and tetragonal ZrO_2 phase (see Figure 1c). The RDF of CZ50 and O-CZ50 are plotted as shown in Figure S2 in the SI. The RDFs Ce−Ce, Zr−Zr, and Ce−Zr of CZ50 and O-CZ50 are similar, i.e., ∼3.8 Å for the first peak, ∼5.3 Å for the second peak, ∼6.5 Å for the third peak, and so on. But in O-CZ50, the RDF of Ce(Zr)−Ce(Zr) at ∼3.8 Å shows equal intensity and a narrow peak, which suggests a very ordered mixing of cations in the presence of O-CZ50. In CZ50, a broad peak of low intensity is present at 3.8−4.2 Å and the Zr−Zr and Ce−Ce peaks at 3.8 Å are the strongest, which indicates that Zr and Ce are individually clustered in CZ50. The structure difference between O(R)-CZ50 and CZ50 can also be seen clearly from the simulated XRD patterns in Figure 1d, where O(R)-CZ50 exhibit typical cubic phase patterns with the major peak (2θ) at 29° corresponding to the crystal plane indices of (111). This differs from the major peaks of CZ50 that comprise two groups, a monoclinic lattice with a peak at 28.6° and a tetragonal lattice with peaks at 30.5° and 35.5°.

Since the Ce_2O_3−ZrO_2 edge of the ternary phase diagram contains the major low-energy phases, we then plot in Figure 1e the thermodynamic convex hull for $Ce_xZr_yO_{2y+3/2x}$ phases using Ce_2O_3 and ZrO_2 as the energy zero reference at the same μ(O) = −2.33 eV. We found that there were three convex points at Ce^{3+} concentration being 50% (ΔG_f = −2.41 eV), 60% (R-CZ60, ΔG_f = −2.15 eV, Figure 1f), and 80% (R-CZ80, ΔG_f = −1.10 eV, Figure 1g). It should be mentioned that even when μ(O) is reduced to 1.75 eV corresponding to Ce_2O_3 in thermodynamic equilibrium with CeO_2 (1400 K and 1 atm pressure), these three phases are still the convex points. In addition, we compared the disproportionation ΔG_d of R-CZ75 and R-CZ66, which are only 0.05 and 0.09 eV (eq 3), respectively, with respect to R-CZ60 and R-CZ80. This suggests that the stabilities are quite close across these concentrations with Ce^{3+} being 60−80%. Consistently, the

Table 1. Structural Properties for the Identified Global Minima of Four CZO Compositions from SSW-NN

[a]name	R-CZ50	R-CZ60	R-CZ80	CZ50
[b]$N_{(Ce/Zr/O)}$	16/16/56	12/8/34	24/6/48	4/4/16
[c]***a***	10.84	13.32	12.47	5.39
b	10.84	6.74	11.82	5.44
c	10.84	10.30	9.59	10.64
α	90	77.46	105.34	94.10
β	90	70.92	72.47	90
γ	90	99.75	85.93	90
[d]CN(Ce)	8	6.83	6.25	8
CN(Zr)	6	6	6	7
[e]$G_{Ov(4Zr)}^{ad}$	0.40 eV			
$G_{Ov(1Ce3Zr)}^{ad}$		1.17 eV		
$G_{Ov(2Ce2Zr)}^{ad}$		1.33 eV	1.21 eV	
$G_{Ov(4Ce)}^{ad}$			1.78 eV	

[a]R-CZx are x% Ce^{3+}-containing CZO; CZ50 is 50% Ce^{4+}-containing CZO. [b]$N_{(Ce/Zr/O)}$ are Ce, Zr, and O atom numbers in a conventional cell. [c]The lattice parameters (***a***, ***b***, ***c***, ***α***, ***β***, ***γ***) of the conventional cell. [d]CN(Ce) and CN(Zr) are the average coordination numbers (CNs) of cations with the first-shell O atoms. [e]G_{Ov}^{ad} is the O_v formation energy at different O_v sites calculated by n = 1 in eq 2.

https://doi.org/10.1021/jacs.4c01285
J. Am. Chem. Soc. XXXX, XXX, XXX−XXX

GM structures of them all exhibit the characteristics of cubic phases in XRD (Figure S3 in the SI).

R-CZ60 and R-CZ80 share great similarity with R-CZ50. For example, the coordination numbers of Zr in R-CZ60 and R-CZ80 are always 6, suggesting that O_v tends to stay close to Zr, if possible. Due to the increased Ce content, there are O_v neighboring Ce, and thus, the average coordination numbers of Ce in R-CZ60 and R-CZ80 are reduced compared to R-CZ50, being 6.83 and 6.25, respectively. Specifically, these O_v can be categorized according to the number of Ce and Zr atoms surrounding the O_v, namely, one Ce and three Zr (1Ce3Zr), 2Ce2Zr, 3Ce1Zr, and 4Ce. In R-CZ60, there are 66.7% O_v(1Ce3Zr) and 33.3% O_v(2Ce2Zr); in R-CZ80, there are 50% O_v(2Ce2Zr) and 50% O_v(4Ce). In companion with the O_v generation, a significant portion of the O atoms are off the cubic lattice position. In particular, the interstitial oxygen atoms (two coordinated O) as reported by the literature[48] are present in the R-CZ60 GM structure (Figure 1f indicated by the arrow), although at a low content (2.94%). In addition, with the increased Ce^{3+} content, the cubic lattice is lengthened and distorted, as reflected in the simulated XRD in Figure 1d. For the 29° peak, the (111) peak of the cubic phase splits into two major peaks in R-CZ60 and evolves into a series of small peaks between 27.7 and 29° in R-CZ80. The lattice parameters of R-CZ80 are 12.47, 11.82, and 9.59 Å, which are significantly lengthened compared to those of R-CZ50 (7.67 Å, see Table 1).

3.2. Thermodynamics of R-CZ50, R-CZ60, and R-CZ80. With the bulk structure determined, we then evaluated the OSC of the three thermodynamically stable CZO at high temperatures, i.e., R-CZ50, R-CZ60, and R-CZ80. This can be done by filling all of the O_v (with O atoms) and computing the average O_v formation energies G^{θ}_{ad} (see Methods eq 2) in their conventional cell (lattice parameters listed in Table 1), a thermodynamics value to measure the OSC. We found that the G^{θ}_{ad} required for the full reduction of these stable CZO phases are 0.40 eV (R-CZ50), 0.82 eV (R-CZ60), and 1.56 eV (R-CZ80; these values are all lower than G^{θ}_{ad} = 2.19 eV, in cubic CeO_2 from our calculations and from the literature[49]). This suggests that O_v(Zr) is preferable for storing oxygen with a low G_{ad}(O), and O_v(Ce) bonds to O strongly and is not desirable for oxygen storage.

We further evaluated the differential adsorption of O in R-CZ50 and R-CZ60 at different temperatures and pressures of O_2. In these calculations, we fix the cation position and use SSW to identify the best O anion distribution at different O_v concentrations (adding O atoms one by one). As shown in Figure 2, the isochemical potential curves can be utilized to determine the favorable phases under different reaction conditions as controlled by O chemical potential. In the R-CZ50 diagram (Figure 2a), when the temperature is lower than 655 K at standard atmospheric pressure (μ(O) = −0.69 eV), CZO solid solution exists in the form of O-CZ50, and it is not until 1100 K (μ(O) = −1.26 eV), all of the oxygen can be fully released in forming R-CZ50. The OSC window thus spans 445 K, from 655 to 1100 K. We note that the gas-phase reference error of the PBE functional for O_2 might contribute an additional 0.23 eV uncertainty on the formation energy of O_v.[50−53] This may shift the window boundary by about ∼70 K in the phase diagram, which indicates uncertainty, as the DFT functional is not critical in this system. Experimentally, it has been measured by Sugiura[13] that at 773 K in air, the OSC of R-CZ50 is 89% (the star symbol in Figure 2a), which agrees with the value (87.5%) from our phase diagram.

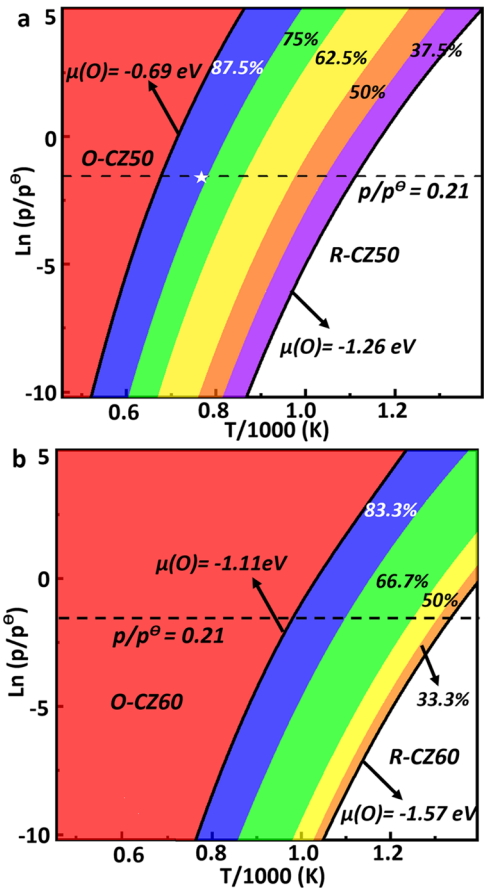

Figure 2. Thermodynamics diagrams of R-CZ50 (a) and R-CZ60 (b) under different conditions. Cationic positions are kept fixed in constructing the thermodynamics diagrams. The white star indicates the experimental condition (773 k and 1 atm).

On the other hand, for R-CZ60, as shown in Figure 2b, the OSC window spans only 340 K and shifts to higher temperature ends, from 980 K (μ(O) = −1.11 eV) to 1320 K (μ(O) = −1.57 eV). A simple comparison can thus be done for two CZO samples at the same temperature: when O-CZ50 fully releases all stored oxygen to R-CZ50 (1100 K), only 33.3% oxygen can be released from O-CZ60 to a partially oxidized form (66.6% oxygen-filled R-CZ60).

The average O_v formation energy for R-CZ80 is the highest of the three components at 1.85 eV; thus, its OSC window spans even smaller, being 320 K, from 1540 to 1860 K at standard atmospheric pressure (the detail can be seen in Figure S4 in the SI). Its high OSC window has no overlap with the OSC window of R-CZ50 at all—even when O-CZ50 fully releases oxygen to R-CZ50, O-CZ80 cannot provide oxygen at the same condition. R-CZ80 is thus an OSC material only at very high temperatures (>1540 K).

Our thermodynamics data on CZO may help to rationalize the CZO obtained in experiments. As shown in Figure 3, we reproduce the experimental XRD of CZO samples obtained under different synthetic conditions.[1] The CZO samples, e.g., 50% Ce-containing CZO,[54] prepared with the coprecipitation method from Ce^{3+} and Zr^{4+} salts at low temperatures (e.g., under 873 K, blue and green lines) exhibit broad XRD peaks at the characteristic 28−31° region. It was suggested that two

https://doi.org/10.1021/jacs.4c01285
J. Am. Chem. Soc. XXXX, XXX, XXX−XXX

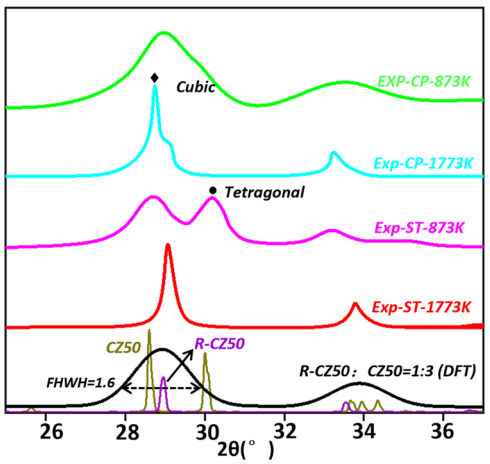

Figure 3. Experimental (Exp)[1] and theoretical XRD patterns for 50% Ce-containing CZO. The curves correspond to the samples synthesized using the coprecipitation (CP) method calcinated at 873 K (green line) and 1773 K (cyan line) and the solvent thermal (ST) method at 873 K (pink line) and 1773 K (cyan line). The theoretical XRD is generated by using two likely phases (R-CZ50 and CZ50) at the R-CZ50/CZ50 ratio of 1:3 (black line) based on DFT lattices (also see Figure 1d). The width (FWHW = 1.6) of the Gaussian function is applied to fit the experimental shape.

phases, cubic and tetragonal phases, are present, although both are not well crystallized.[55] After annealing to 1773 K, the XRD peaks at the region become much sharper, which can align with that of the cubic phase (cf. ∼29° see Figure 1d), suggesting the tetragonal to cubic phase transition. On the other hand, the samples prepared under the solvent thermal method[1] at 873 K show two narrower peaks at 29 and 30.5° in XRD (pink line), suggesting that the solvent thermal method can yield better-crystallized solids with both cubic (c.f. 29°) and tetragonal phases (c.f. 30.5 and 35.5, Figure 1d). The sample exhibits a sharp single peak at 29° after annealing to 1773 K,[12] characterizing as a single cubic phase (red line) with high crystallization, similar to that using the coprecipitation method (green line).

The experimental results suggest that 50% Ce-containing CZO samples do have two likely crystal forms at low temperatures (873 K), independent of the synthetic methods. From our data, R-CZ50, the GM at high temperatures (Figure 1a), has an XRD pattern of the cubic phase that is consistent with the 1773 K XRD from experiments. The oxidation of R-CZ50 will lead to O-CZ50, which is however not the most stable structure when all Ce becomes Ce^{4+}. Instead, CZ50, a mixed monoclinic and tetragonal phase from simulated XRD (Figure 1d), is more stable (Figure 1c), where Ce and Zr cations are aggregated into separate domains (a detailed structure difference between R-CZ50 and CZ50 can be found in the SI). By simulating XRD patterns containing different ratios of R-CZ50 and CZ50, including 3:1, 1:1, and 1:3 (also see Figure S5 in the SI), we found that, as shown in Figure 3, black line, the XRD for a mixed-phase catalyst with R-CZ50/CZ50 = 1:3, which was the adjusted width (FWHW = 1.6) of the Gaussian function, can best reproduce the experimental XRD pattern at 873 K, which contains a single broad peak at 28−31°. The mixing of R-CZ50 and CZ50 as the model for low-temperature CZO not only rationalizes that both cubic

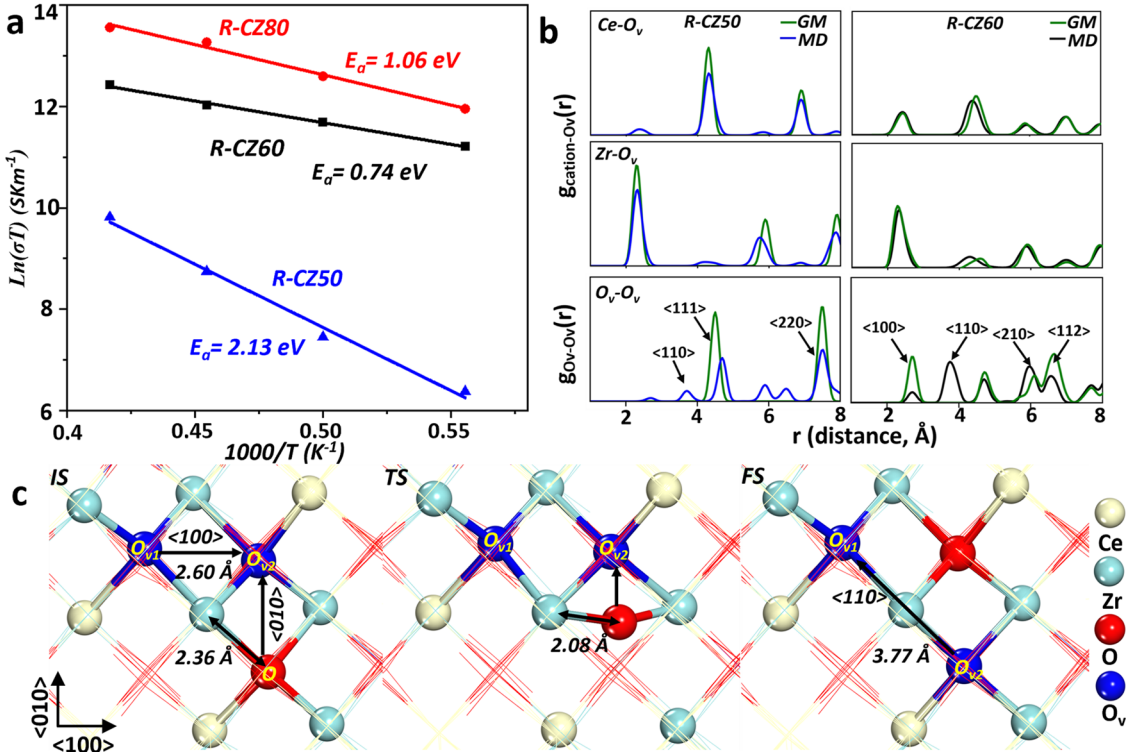

Figure 4. Anion migration kinetics. (a) The apparent oxygen ion diffusion activation energy of R-CZ50, R-CZ60, and R-CZ80 by linear fitting of the diffusion rate against temperature using the Arrhenius plot. (b) Radial distribution function $g(r)$ of the cation (Zr, Ce)−O_v and O_v−O_v pairs at 2400 K from the averaged snapshots of MD simulations (blue and black lines) to compare with their GM structures (green lines). (c) The snapshots of the lowest energy O_v diffusion pathway from ⟨100⟩ to ⟨110⟩ in R-CZ60. Both peaks in the series O_v belong to the group of O_v(1Ce3Zr).

https://doi.org/10.1021/jacs.4c01285
J. Am. Chem. Soc. XXXX, XXX, XXX−XXX

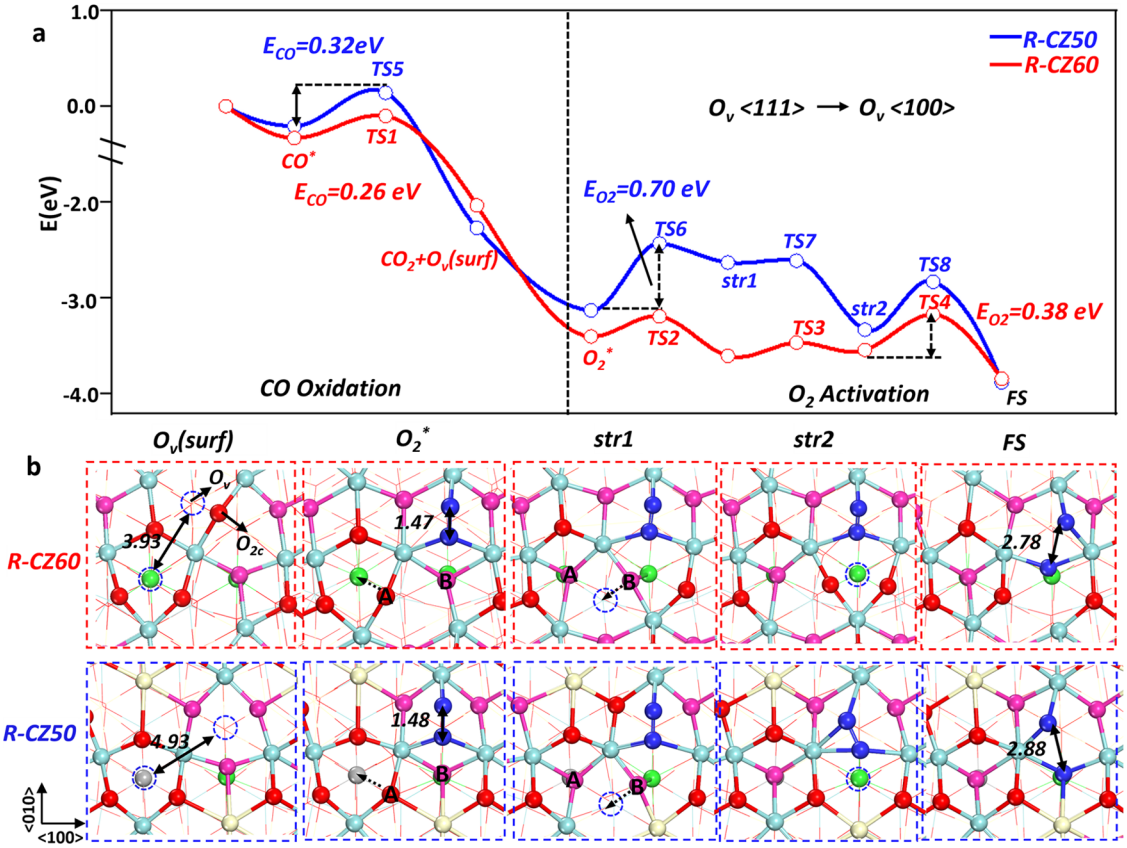

Figure 5. Catalytic CO oxidation on two CZO surfaces. (a) The energy reaction profiles of CO oxidation and O_2 activation at the (201) surface of 33.3% O-filled R-CZ60 and the 25% O-filled (111) surface of R-CZ50. (b) The key structures involved in O_2 activation in R-CZ60 and R-CZ50. The blue dashed circles and balls represent O_v and O (in O_2), respectively. Pink balls: the subsurface layer of O atoms; red balls: the top layer of O atoms; green balls: the second layer of Ce; gray balls: the second layer of Zr. Dashed arrows represent the direction of oxygen diffusion.

and tetragonal phases are present in experimental samples but also points out that the monoclinic phase of ZrO_2 contributes to the broad peak at 28.6°. The phase transition from low (873 K) to high temperatures (1773 K) is thus the CZ50 to R-CZ50 structure change, which involves both the creation of O_v and the migration of the Ce/Zr cation in the lattice.

3.3. Anion Migration Kinetics. Apart from the thermodynamics governing the OSC window, the migration rate of the O anion should also affect the apparent OSC in the experiment at a given working temperature. By performing long-time MD simulations from 1800 to 2400 K (Figure 4a), we investigated the diffusion ability of the O anion for R-CZ50, R-CZ60, and R-CZ80. The apparent oxygen ion diffusion activation energy (E_a) is thus obtained by linear fitting of the diffusion rate against the temperature using the Arrhenius plot shown in Figure 4a. The E_a values are 2.13, 0.74, and 1.06 eV for R-CZ50, R-CZ60, and R-CZ80, respectively. Interestingly, R-CZ60 has the smallest E_a, and R-CZ50 has the highest one, which suggests that R-CZ60 is the material with the fastest anion diffusion.

To better understand the diffusion behavior of bulk oxygen, we extracted 100 structure snapshots of R-CZ50 and R-CZ60 from their MD trajectories, one per 100 ps, and after the local optimization, we plotted their averaged radial distribution functions (RDF),[56] $g(r)$, for Zr−O_v, Ce−O_v, and O_v−O_v pairs, as shown in Figure 4b (the RDF of R-CZ80 can be seen in Figure S6 in the SI). The RDFs in Figure 4b show that the cation−O_v peaks (Figure 4b top and middle panels) appear at similar positions compared with their GMs, i.e., ∼ 2.5 Å for the first cation−O_v peak, ∼4.5 Å for the second, and so on. It is obvious that for R-CZ50, the atoms of O_v originally present exclusively near Zr diffuse to the neighbor of Ce in finite-temperature MD simulations, as reflected by the increase of the Ce−O_v peak at ∼2.5 Å.

For the RDF of O_v−O_v pairs (Figure 4b bottom panel), the distributions are more complex, where R-CZ50 and R-CZ60 exhibit distinct features. In R-CZ50, the two peaks in ⟨111⟩ (∼4.7 Å) and ⟨220⟩ (∼7.7 Å) directions exhibit the strongest intensity. The minor peak at ⟨110⟩ (∼3.8 Å) suggests that the six-coordinated Zr with two O_v is indeed present during O_v migration. In R-CZ60, the primary feature is three peaks in the ⟨110⟩ (∼3.8 Å), ⟨210⟩ (∼5.9 Å), and ⟨112⟩ (∼6.5 Å) directions. The ⟨110⟩ peak is originally not present in the RDF for the GM of R-CZ60 but turns out to be the strongest peak during O_v migration, which is accompanied by the weakening of the ⟨100⟩ peak in R-CZ60 GM. The peak corresponding to the ⟨210⟩ direction exhibits a similar phenomenon, not being prominent in GM, but becomes the second strongest peak during migration, replacing the original strong ⟨112⟩ peak. This is consistent with the previously reported results for O diffusion in Y-doped ZrO_2 that diffusion along the ⟨112⟩ direction is unfavorable because O_v tends not to be adjacent to the other O_v during migration.[57]

To understand the process of O_v in diffusion to form ⟨110⟩ direction pairs, we select the GM of R-CZ60 as the IS and explore the 20 elementary diffusion steps (diffusing along ⟨100⟩, ⟨010⟩, and ⟨001⟩) to form ⟨110⟩ O_v−O_v pairs. The lowest energy pathway is thus identified and is shown in Figure

https://doi.org/10.1021/jacs.4c01285
J. Am. Chem. Soc. XXXX, XXX, XXX−XXX

4c. In this reaction, the O_v diffuses from O_v(1Ce3Zr) to another O_v(1Ce3Zr), and the barrier is only 0.75 eV, which is in line with the low activation barrier fitted from the MD simulation. As shown in Figure 4c, IS for the lowest energy pathway, two O_v(1Ce3Zr), i.e., O_{v1} and O_{v2}, being 2.60 Å apart, are located along the ⟨100⟩ direction. In the reaction, oxygen migrates toward O_{v2} along the ⟨010⟩ direction, shortening the length of the Zr−O bond from 2.36 to2.08 Å at the TS, eventually occupying the O_{v2} and forming a pair of O_{v1}−O_{v2} along the ⟨110⟩ direction. It might be mentioned that among all 20 pathways, the highest energy barrier is 1.70 eV, where O_v diffuses from O_v(1Ce3Zr) to O_v(3Ce1Zr).

We note that the interstitial oxygen atoms are routinely observed in our MD trajectories and contribute to O_v diffusion. For example, at 2400 K MD trajectories, the average percentages of interstitial oxygen in R-CZ50, R-CZ60, and R-CZ80 are counted to be 0.086, 2.20, and 1.58%, respectively (a typical snapshot for interstitial oxygen diffusion is described in Figure S7 in the SI).

In R-CZ50, the elementary diffusion step of O_v is much simpler compared to R-CZ60, since all O_v being to O_v(4Zr) (Table 1) and Ce/Zr distribution has a high symmetry. When O_v diffusion starts, O_v first migrates from O_v(4Zr) to O_v(2Ce2Zr) with a barrier of 0.49 eV. Next, O_v has to move from O_v(2Ce2Zr) to O_v(4Ce), which needs to overcome a very high barrier of 2.42 eV. The reason for the large difference in the diffusion barrier between R-CZ50 and R-CZ60 can thus be attributed to the different O_v formation energies along the diffusion pathway, which inevitably leads to the local accumulation of O_v. In R-CZ50, the diffusion needs to pass through O_v(2Ce2Zr) and O_v(4Ce), where O_v(4Ce) is 1.65 eV less stable than O_v(2Ce2Zr). However, in R-CZ60, O_v can diffuse from one O_v(1Ce3Zr) to another O_v(1Ce3Zr), and the energy difference between them is less than 0.33 eV.

3.4. CO Oxidation Activity. Based on the previous understandings, we finally selected two CZOs, R-CZ50 and R-CZ60, and investigated their CO oxidation activity. Since O_v should be gradually filled until O_v creation is kinetically prohibited during CO oxidation, we first carried out a series of calculations to evaluate the most likely bulk and surface O_v concentration for the two CZOs under reaction conditions. ΔE_r (eq 4) is utilized to evaluate whether a particular lattice/surface O can be removed under reaction conditions. Taking the most stable surface as the model, R(O)-CZ50 (111) and R(O)-CZ60 (201), we found that with the increase of O content, ΔE_r drops from −4.07 eV in O-CZ50 to −2.27 eV in the R-CZ50 (111) surface, while it drops from −3.24 eV in O-CZ60 to −2.03 eV in 33.3% O-filled R-CZ60 and becomes positive if O_v is further created. To allow for the CO oxidation cycle, we therefore select the 25% O-filled (111) face of R-CZ50 and the (201) face of 33.3% O-filled R-CZ60 as the final state models for the two CZO catalysts. The details of the surface O_v distribution are shown in Figure S8. In Figure S9 in the SI, we show that the choice of proper surface O_v concentration is critical. For example, on the surfaces of fully oxidized O-CZ50 and O-CZ60 O, CO can be readily oxidized with very low barriers (0 and 0.17 eV) due to the high activity of surface O. In the following, we elaborate on the lowest energy pathways for CO oxidation on two CZO surfaces.

3.4.1. CO Oxidation on 33.3% O-Filled R-CZ60(210). Figure 5a shows the energy profile of CO oxidation, which can be divided into two parts: CO oxidation and O_2 activation. For the CO oxidation process, CO is first adsorbed on the Zr site with 0.33 eV adsorption energy and then reacts with its neighboring O (2.54 Å away, see Figure S10 in the SI), where the TS (TS1) is achieved when the CO and O distance is 1.75 Å. The CO_2 formation has a barrier of 0.26 eV and releases energy by 2.03 eV. After the reaction, two close-neighboring O_v are created on the surface due to the formation of an interstitial O (O_{2c} Figure 5b) after local relaxation.

For the O_2 activation process, the closest O_v pair spaced 3.93 Å apart along ⟨110⟩ (Figure 5b) is involved in facilitating O−O bond breaking. In the reaction, O_2 can be adsorbed at one O_v site, noted as O_2*, with a significant adsorption energy (1.37 eV), with the O−O distance being 1.47 Å. Then, one neighboring O atom (labeled as atom A in Figure 5b top panel) migrates from the top layer to the subsurface layer to fill O_v(1Ce3Zr). The reaction is from O_2* to str1 with TS2. Next, another nearby O atom (B atom in Figure 5b) moves from the subsurface layer to heal the surface O_v(1Ce3Zr) site. After the fast diffusion of surface O, the O−O bond then breaks by overcoming a barrier of 0.38 eV at TS4, and the dissociation reaction is exothermic by 0.30 eV. After the reaction, the O_v pair along the ⟨110⟩ direction is healed by two dissociated O atoms.

3.4.2. CO Oxidation on 25% O-Filled R-CZ50(111). Similar to that in R-CZ60, the CO reaction with one surface O of R-CZ50(111) is also facile with a low barrier of 0.32 eV. The major difference lies in the O_2 activation, as there are no close O_v pairs in the R-CZ50 surface. In the O_2 activation, O_2 is first adsorbed on a surface O_v site along the ⟨100⟩ direction, with the O−O distance being 1.48 Å. Then, the O atom diffusion process is basically the same as those in R-CZ60, except that str1 involves O_v(2Ce2Zr) and str2 involves O_v(2Ce2Zr). Obviously, O_v(2Ce2Zr) is much less stable compared to O_v(1Ce3Zr) in R-CZ60. The subsequent O_2 dissociation is also facile with only a 0.50 eV barrier, but the overall barrier is higher (0.70 eV), originating from the unfavorable O_v diffusion.

From the reaction profile in Figure 5, we can see that the elementary step of CO oxidation has a low barrier on both R-CZ50 and R-CZ60 surfaces, although the CO + O barrier on R-CZ60 is still 0.06 eV lower than that on R-CZ50. It is the activation of the O_2 complex that dictates the reaction barrier difference of CO oxidation. From our energy pathway, O_2 activation requires a surface O_v pair and thus is influenced by the O_v distribution, a structural property dictated by the Ce/Zr ratio. On the R-CZ60 surface, O_v is more stable and the closest O_v pairs are distributed along the ⟨110⟩ direction. O_2 can dissociate by the fast diffusion of stable O_v(1Ce3Zr) with only a 0.38 eV barrier. On the R-CZ50 surface, O_v is less stable and O_v is distal with the other O_v. To allow for O_2 dissociation, O_v diffusion between surface and subsurface layers is necessary, which is, however, kinetically difficult with a barrier of 0.70 eV due to the involvement of less stable O_v(2Ce2Zr). It is the O anion diffusion that causes a distinct CO oxidation activity for R-CZ50 and R-CZ60.

Our theoretical results help to provide atomic-level insights into a large volume of experimental observations. For example, Boaro et. al found that catalysts containing 50−80% Ce have the best CO oxidation activity.[21] This could be rationalized because first, O_2 activation is much easier on the high-Ce-content CZO compared to 50% Ce-containing CZO, and second, the CO + O reaction is also easier on higher-Ce-content CZO. On the other hand, above 80% Ce content, the CZO is not stable (Figure 1), and the OSC ability also

https://doi.org/10.1021/jacs.4c01285
J. Am. Chem. Soc. XXXX, XXX, XXX−XXX

diminishes, which leads to a decrease in catalysis performance. For catalytic oxidation, not only is the oxygen removal (CO + O reaction) important, but the O_2 dissociation is also critical, where the presence of geometrically close O_v pairs is a must. From our results, only Ce content above 60% (R-CZ60, R-CZ80) starts to exhibit a high density of low-energy O_v pairs (along ⟨110⟩, Figure 5b). It is therefore not surprising that the high OSC ability of R-CZ50 does not bring any higher catalytic oxidation performance. Furthermore, the importance of oxygen diffusion to catalytic oxidation can also explain the observed activity variation for catalysts synthesized using different methods. Our results indicate that the fast oxygen diffusion occurs exclusively along ⟨100⟩ in the cubic phase, which implies that poorly crystallized CZO and the mixing of the monoclinic phase (as that in CZ50) should deteriorate the catalytic performance. Since the solvent thermal method can yield better crystalline CZO (Figure 3), it is reasonable that solvent thermal-synthesized CZO does show a T_{50} of 688 K for CO oxidation, being much lower than that of the coprecipitation sample (T_{50} exceeds 873 K).[1]

4. CONCLUSIONS

This work represents the first attempt to explore the global potential energy surface of an industrially important ternary Ce−Zr−O oxide, where bivalent states (3+ and 4+) are available for Ce. By constructing a Ce−Zr−O G-NN potential with the SSW global optimization algorithm, we identify the ternary phase diagram and reveal three key compositions that are thermodynamically stable at typical high temperatures of calcination, namely, R-CZ50, R-CZ60, and R-CZ80. The thermodynamics of OSC and kinetics governing the migration of the octahedral CZO are then determined.

We show that the Ce/Zr cationic position as dictated by thermodynamics influences strongly the properties of CZO, since O_v is preferably generated near Zr, and the increase of first-neighbor Ce cations near O_v dramatically hampers the O_v creation. Notably, R-CZ60, despite lower OSC (33.3%) compared to R-CZ50 (100% OSC), owns the best O anion diffusion kinetics due to the ability to create low-energy O_v pairs. The O anion diffusion in R-CZ60 has an apparent barrier as low as 0.74 eV, which further leads to the highest CO oxidation activity (energy barrier of 0.38 eV). Our results highlight the great potential of R-CZ60 in diverse applications, both as the OSC material and catalysts. With the emergence of machine learning atomic simulations, we believe that the novel structures and properties predicted via global potential energy surface exploration could offer valuable insights into the design of new materials with desirable properties for target applications.

■ ASSOCIATED CONTENT

Supporting Information

The Supporting Information is available free of charge at https://pubs.acs.org/doi/10.1021/jacs.4c01285.

Data set summary of the Ce−Zr−O ternary G-NN potential; benchmark of the G-NN potential against DFT calculations; benchmark of thermodynamics among different computational methods; RDF of the Ce−Ce, Zr−Zr, and Zr−Ce of CZ50 and R-CZ50 and Ce−O_v, Zr−O_v, and O_v−O_v in R-CZ80; simulated XRD patterns for R-CZ66 and R-CZ75; snapshots of CO oxidation on R-CZ50 and R-CZ60 surfaces; and XYZ coordinates of R-CZ60, R-CZ80, and CZ50 (PDF)

■ AUTHOR INFORMATION

Corresponding Authors

Cheng Shang − *Collaborative Innovation Center of Chemistry for Energy Materials (iChEM), Shanghai Key Laboratory of Molecular Catalysis and Innovative Materials, Key Laboratory of Computational Physical Science, Department of Chemistry, Fudan University, Shanghai 200433, China; Shanghai Qi Zhi Institution, Shanghai 200030, China;* orcid.org/0000-0001-7486-1514; Email: cshang@fudan.edu.cn

Zhi-Pan Liu − *Collaborative Innovation Center of Chemistry for Energy Materials (iChEM), Shanghai Key Laboratory of Molecular Catalysis and Innovative Materials, Key Laboratory of Computational Physical Science, Department of Chemistry, Fudan University, Shanghai 200433, China; Key Laboratory of Synthetic and Self-Assembly Chemistry for Organic Functional Molecules, Shanghai Institute of Organic Chemistry, Chinese Academy of Sciences, Shanghai 200032, China; Shanghai Qi Zhi Institution, Shanghai 200030, China;* orcid.org/0000-0002-2906-5217; Email: zpliu@fudan.edu.cn

Authors

Yao Peng − *Collaborative Innovation Center of Chemistry for Energy Materials (iChEM), Shanghai Key Laboratory of Molecular Catalysis and Innovative Materials, Key Laboratory of Computational Physical Science, Department of Chemistry, Fudan University, Shanghai 200433, China*

Xia-Lan Si − *Collaborative Innovation Center of Chemistry for Energy Materials (iChEM), Shanghai Key Laboratory of Molecular Catalysis and Innovative Materials, Key Laboratory of Computational Physical Science, Department of Chemistry, Fudan University, Shanghai 200433, China*

Complete contact information is available at: https://pubs.acs.org/10.1021/jacs.4c01285

Author Contributions

The manuscript was written through contributions of all authors. All authors have given approval for the final version of the manuscript.

Notes

The authors declare no competing financial interest.

■ ACKNOWLEDGMENTS

This work received financial support from the National Science Foundation of China (12188101, 22122301, 22033003, 91745201, 91945301, 92145302, and 92061112), the Fundamental Research Funds for the Central Universities (20720220011), the National Key Research and Development Program of China (2018YFA0208600), and the Tencent Foundation for XPLORER PRIZE.

■ REFERENCES

(1) Ding, Y.; Wang, Z.; Guo, Y.; Guo, Y.; Wang, L.; Zhan, W. A novel method for the synthesis of $Ce_xZr_{1-x}O_2$ solid solution with high purity of κappa phase and excellent reactive activity. *Catal. Today* **2019**, *327*, 262−270.

(2) Mamontov, E.; Egami, T.; Brezny, R.; Koranne, M.; Tyagi, S. Lattice Defects and Oxygen Storage Capacity of Nanocrystalline Ceria and Ceria-Zirconia. *J. Phys. Chem. B* **2000**, *104*, 11110−11116.

https://doi.org/10.1021/jacs.4c01285
J. Am. Chem. Soc. XXXX, XXX, XXX−XXX

(3) Devaiah, D.; Reddy, L. H.; Park, S.-E.; Reddy, B. M. Ceria–zirconia mixed oxides: Synthetic methods and applications. *Catal. Rev.* **2018**, *60*, 177–277.
(4) Vidal, H.; Kašpar, J.; Pijolat, M.; Colon, G.; Bernal, S.; Cordón, A.; Perrichon, V.; Fally, F. Redox behavior of CeO_2–ZrO_2 mixed oxides: I. Influence of redox treatments on high surface area catalysts. *Appl. Catal., B* **2000**, *27*, 49–63.
(5) *Catalysis by Ceria and Related Materials*; Published by Imperial College Press and Distributed by World Scientific Publishing Co, 2002; Vol. 2.
(6) Arai, S.; Muto, S.; Murai, J.; Sasaki, T.; Ukyo, Y.; Kuroda, K.; Saka, H. Valence Change of Cations in Ceria-Zirconia Solid Solution Associated with Redox Reactions Studied with Electron Energy-Loss Spectroscopy. *Mater. Trans.* **2004**, *45*, 2951–2955.
(7) Montini, T.; Melchionna, M.; Monai, M.; Fornasiero, P. Fundamentals and Catalytic Applications of CeO_2-Based Materials. *Chem. Rev.* **2016**, *116*, 5987–6041.
(8) Kaspar, J.; Fornasiero, P.; Balducci, G.; Di Monte, R.; Hickey, N.; Sergo, V. Effect of ZrO_2 content on textural and structural properties of CeO_2–ZrO_2 solid solutions made by citrate complexation route. *Inorg. Chim. Acta* **2003**, *349*, 217–226.
(9) Carter, J. H.; Abdel-Mageed, A. M.; Zhou, D.; Morgan, D. J.; Liu, X.; Bansmann, J.; Chen, S.; Behm, R. J.; Hutchings, G. J. Reversible Growth of Gold Nanoparticles in the Low-Temperature Water–Gas Shift Reaction. *ACS Nano* **2022**, *16*, 15197–15205.
(10) Carter, J. H.; Liu, X.; He, Q.; Althahban, S.; Nowicka, E.; Freakley, S. J.; Niu, L.; Morgan, D. J.; Li, Y.; Niemantsverdriet, J. W.; Golunski, S.; Kiely, C. J.; Hutchings, G. J. Activation and Deactivation of Gold/Ceria–Zirconia in the Low-Temperature Water–Gas Shift Reaction. *Angew. Chem., Int. Ed.* **2017**, *56*, 16037–16041.
(11) Stere, C. E.; Anderson, J. A.; Chansai, S.; Delgado, J. J.; Goguet, A.; Graham, W. G.; Hardacre, C.; Taylor, S. F. R.; Tu, X.; Wang, Z.; Yang, H. Non-Thermal Plasma Activation of Gold-Based Catalysts for Low-Temperature Water–Gas Shift Catalysis. *Angew. Chem., Int. Ed.* **2017**, *56*, 5579–5583.
(12) Parastaev, A.; Muravev, V.; Huertas Osta, E.; van Hoof, A. J. F.; Kimpel, T. F.; Kosinov, N.; Hensen, E. J. M. Boosting CO_2 hydrogenation via size-dependent metal–support interactions in cobalt/ceria-based catalysts. *Nat. Catal.* **2020**, *3*, 526–533.
(13) Sugiura, M. Oxygen Storage Materials for Automotive Catalysts: Ceria-Zirconia Solid Solutions. *Catal. Surv. Asia* **2003**, *7*, 77–87.
(14) Roh, H.-S.; Potdar, H. S.; Jun, K.-W.; Kim, J.-W.; Oh, Y.-S. Carbon dioxide reforming of methane over Ni incorporated into Ce–ZrO_2 catalysts. *Appl. Catal., A* **2004**, *276*, 231–239.
(15) Kishimoto, H.; Omata, T.; Otsuka-Yao-Matsuo, S.; Ueda, K.; Hosono, H.; Kawazoe, H. Crystal structure of metastable κ-$CeZrO_4$ phase possessing an ordered arrangement of Ce and Zr ions. *J. Alloys Compd.* **2000**, *312*, 94–103.
(16) Urban, S.; Djerdj, I.; Dolcet, P.; Chen, L.; Möller, M.; Khalid, O.; Camuka, H.; Ellinghaus, R.; Li, C.; Gross, S.; Klar, P. J.; Bernd, S.; Over, H. In Situ Study of the Oxygen-Induced Transformation of Pyrochlore $Ce_2Zr_2O_{7+x}$ to the κ-$Ce_2Zr_2O_8$ Phase. *Chem. Mater.* **2017**, *29*, 9218–9226.
(17) Hui, Z.; Nicolas, G.; Françoise, V.; Michèle, P. Preparation and electrical properties of a pyrochlore-related $Ce_2Zr_2O_{8-x}$ phase. *Solid State Ionics* **2003**, *160*, 317–326.
(18) Wang, H.-F.; Guo, Y.-L.; Lu, G.-Z.; Hu, P. Maximizing the Localized Relaxation: The Origin of the Outstanding Oxygen Storage Capacity of κ-$Ce_2Zr_2O_8$. *Angew. Chem., Int. Ed.* **2009**, *48*, 8289–8292.
(19) Madier, Y.; Descorme, C.; Le Govic, A. M.; Duprez, D. Oxygen Mobility in CeO_2 and $Ce_xZr_{(1-x)}O_2$ Compounds: Study by CO Transient Oxidation and $^{18}O/^{16}O$ Isotopic Exchange. *J. Phys. Chem. B* **1999**, *103*, 10999–11006.
(20) Si, R.; Zhang, Y.-W.; Li, S.-J.; Lin, B.-X.; Yan, C.-H. Urea-Based Hydrothermally Derived Homogeneous Nanostructured $Ce_{1-x}Zr_xO_2$ (x = 0–0.8) Solid Solutions: A Strong Correlation between Oxygen Storage Capacity and Lattice Strain. *J. Phys. Chem. B* **2004**, *108*, 12481–12488.
(21) Boaro, M.; de Leitenburg, C.; Dolcetti, G.; Trovarelli, A. The Dynamics of Oxygen Storage in Ceria–Zirconia Model Catalysts Measured by CO Oxidation under Stationary and Cycling Feedstream Compositions. *J. Catal.* **2000**, *193*, 338–347.
(22) Conesa, J. C. Surface anion vacancies on ceria: Quantum modelling of mutual interactions and oxygen adsorption. *Catal. Today* **2009**, *143*, 315–325.
(23) Li, H.-Y.; Wang, H.-F.; Gong, X.-Q.; Guo, Y.-L.; Guo, Y.; Lu, G.; Hu, P. Multiple configurations of the two excess 4f electrons on defective CeO_2(111): Origin and implications. *Phys. Rev. B* **2009**, *79*, No. 193401.
(24) Chen, H.-T.; Chang, J.-G.; Chen, H.-L.; Ju, S.-P. Identifying the O_2 diffusion and reduction mechanisms on CeO_2 electrolyte in solid oxide fuel cells: A DFT + U study. *J. Comput. Chem.* **2009**, *30*, 2433–2442.
(25) Huang, M.; Fabris, S. Role of surface peroxo and superoxo species in the low-temperature oxygen buffering of ceria: Density functional theory calculations. *Phys. Rev. B* **2007**, *75*, No. 081404.
(26) Choi, Y. M.; Abernathy, H.; Chen, H.-T.; Lin, M. C.; Liu, M. Characterization of O_2–CeO_2 Interactions Using In Situ Raman Spectroscopy and First-Principle Calculations. *ChemPhysChem* **2006**, *7*, 1957–1963.
(27) Huang, M.; Fabris, S. CO Adsorption and Oxidation on Ceria Surfaces from DFT + U Calculations. *J. Phys. Chem. C* **2008**, *112*, 8643–8648.
(28) Huang, S.-D.; Shang, C.; Kang, P.-L.; Zhang, X.-J.; Liu, Z.-P. LASP: Fast global potential energy surface exploration. *WIREs Comput. Mol. Sci.* **2019**, *9*, No. e1415.
(29) Shang, C.; Zhang, X.-J.; Liu, Z.-P. Stochastic surface walking method for crystal structure and phase transition pathway prediction. *Phys. Chem. Chem. Phys.* **2014**, *16*, 17845–17856.
(30) Shang, C.; Liu, Z.-P. Stochastic Surface Walking Method for Structure Prediction and Pathway Searching. *J. Chem. Theory Comput.* **2013**, *9*, 1838–1845.
(31) Huang, S.-D.; Shang, C.; Zhang, X.-J.; Liu, Z.-P. Material discovery by combining stochastic surface walking global optimization with a neural network. *Chem. Sci.* **2017**, *8*, 6327–6337.
(32) Ma, S.; Shang, C.; Liu, Z.-P. Heterogeneous catalysis from structure to activity via SSW-NN method. *J. Chem. Phys.* **2019**, *151*, No. 050901.
(33) Kresse, G.; Furthmüller, J. Efficiency of ab-initio total energy calculations for metals and semiconductors using a plane-wave basis set. *Comput. Mater. Sci.* **1996**, *6*, 15–50.
(34) Shang, C.; Liu, Z. P. CeZrO dataset download. http://www.lasphub.com/supportings/Trainfile_CeZrO.tar.gz (accessed March 30, 2024).
(35) Kang, P.-L.; Yang, Z.-X.; Shang, C.; Liu, Z.-P. Global Neural Network Potential with Explicit Many-Body Functions for Improved Descriptions of Complex Potential Energy Surface. *J. Chem. Theory Comput.* **2023**, *19*, 7972–7981.
(36) Shang, C.; Liu, Z. P. CeZrO potential download http://www.lasphub.com/supportings/CeZrO.pot (accessed March 30, 2024).
(37) Perdew, J. P.; Burke, K.; Ernzerhof, M. Generalized Gradient Approximation Made Simple. *Phys. Rev. Lett.* **1996**, *77*, 3865–3868.
(38) Kresse, G.; Joubert, D. From ultrasoft pseudopotentials to the projector augmented-wave method. *Phys. Rev. B* **1999**, *59*, 1758–1775.
(39) Monkhorst, H. J.; Pack, J. D. Special points for Brillouin-zone integrations. *Phys. Rev. B* **1976**, *13*, 5188–5192.
(40) Nolan, M.; Parker, S. C.; Watson, G. W. The electronic structure of oxygen vacancy defects at the low index surfaces of ceria. *Surf. Sci.* **2005**, *595*, 223–232.
(41) Wellendorff, J.; Lundgaard, K. T.; Møgelhøj, A.; Petzold, V.; Landis, D. D.; Nørskov, J. K.; Bligaard, T.; Jacobsen, K. W. Density functionals for surface science: Exchange-correlation model development with Bayesian error estimation. *Phys. Rev. B* **2012**, *85*, No. 235149.
(42) Grimme, S.; Antony, J.; Ehrlich, S.; Krieg, H. A consistent and accurate ab initio parametrization of density functional dispersion

https://doi.org/10.1021/jacs.4c01285
J. Am. Chem. Soc. XXXX, XXX, XXX–XXX

correction (DFT-D) for the 94 elements H-Pu. *J. Chem. Phys.* **2010**, *132*, No. 154104.
(43) Chase, M. W., Jr.NIST-JANAF Themochemical Tables, Fourth Edition *J. Phys. Chem. Ref. Data* 1998, Monograph 9, 1−1951.
(44) Hoover, W. G. Canonical dynamics: Equilibrium phase-space distributions. *Phys. Rev. A* **1985**, *31*, 1695−1697.
(45) Nosé, S. A unified formulation of the constant temperature molecular dynamics methods. *J. Chem. Phys.* **1984**, *81*, 511−519.
(46) Zhang, X.-J.; Shang, C.; Liu, Z.-P. Double-Ended Surface Walking Method for Pathway Building and Transition State Location of Complex Reactions. *J. Chem. Theory Comput.* **2013**, *9*, 5745−5753.
(47) Liu, J.; Zhao, Z.; Xu, C.; Liu, J. Structure, synthesis, and catalytic properties of nanosize cerium-zirconium-based solid solutions in environmental catalysis. *Chin. J. Catal.* **2019**, *40*, 1438−1487.
(48) Summer, A.; Playford, H. Y.; Owen, L. R.; Fisher, J. M.; Kolpin, A.; Thompsett, D.; Walton, R. I. Order and disorder in cerium-rich ceria-zirconia solid solutions revealed from reverse Monte Carlo analysis of neutron and x-ray total scattering. *APL Mater.* **2023**, *11*, No. 031113, DOI: 10.1063/5.0139567.
(49) Wang, H.-F.; Li, H.-Y.; Gong, X.-Q.; Guo, Y.-L.; Lu, G.-Z.; Hu, P. Oxygen vacancy formation in CeO_2 and $Ce_{1-x}Zr_xO_2$ solid solutions: electron localization, electrostatic potential and structural relaxation. *Phys. Chem. Chem. Phys.* **2012**, *14*, 16521−16535.
(50) Christensen, R.; Hansen, H. A.; Vegge, T. Identifying systematic DFT errors in catalytic reactions. *Catal. Sci. Technol.* **2015**, *5*, 4946−4949.
(51) Studt, F.; Abild-Pedersen, F.; Varley, J. B.; Nørskov, J. K. CO and CO2 Hydrogenation to Methanol Calculated Using the BEEF-vdW Functional. *Catal. Lett.* **2013**, *143*, 71−73.
(52) Urrego-Ortiz, R.; Builes, S.; Illas, F.; Calle-Vallejo, F. Gas-phase errors in computational electrocatalysis: a review. *EES Catal.* **2024**, *2*, 157−179.
(53) Grabow, L. C.; Mavrikakis, M. Mechanism of Methanol Synthesis on Cu through CO2 and CO Hydrogenation. *ACS Catal.* **2011**, *1*, 365−384.
(54) Bao, H.; Qian, K.; Chen, X.; Fang, J.; Huang, W. Spectroscopic study of microstructure-reducibility relation of $Ce_xZr_{1-x}O_2$ solid solutions. *Appl. Surf. Sci.* **2019**, *467*−*468*, 361−369.
(55) Liotta, L. F.; Macaluso, A.; Longo, A.; Pantaleo, G.; Martorana, A.; Deganello, G. Effects of redox treatments on the structural composition of a ceria−zirconia oxide for application in the three-way catalysis. *Appl. Catal., A* **2003**, *240*, 295−307.
(56) Guan, S.-H.; Zhang, K.-X.; Shang, C.; Liu, Z.-P. Stability and anion diffusion kinetics of Yttria-stabilized zirconia resolved from machine learning global potential energy surface exploration. *J. Chem. Phys.* **2020**, *152*, No. 094703.
(57) Guan, S.-H.; Shang, C.; Liu, Z.-P. Resolving the Temperature and Composition Dependence of Ion Conductivity for Yttria-Stabilized Zirconia from Machine Learning Simulation. *J. Phys. Chem. C* **2020**, *124*, 15085−15093.

https://doi.org/10.1021/jacs.4c01285
J. Am. Chem. Soc. XXXX, XXX, XXX−XXX